Chapter 6: Short-lived Climate Forces
Supplementary Material

Coordinating Lead Authors:
Sophie Szopa (France), Vaishali Naik (USA)

Lead Authors:
Bhupesh Adhikary (Nepal), Paulo Artaxo (Brazil), Terje Berntsen (Norway), William D. Collins (USA), Sandro Fuzzi (Italy), Laura Gallardo (Chile), Astrid Kiendler-Scharr (Germany/Austria), Zbigniew Klimont (Austria/Poland), Hong Liao (China), Nadine Unger (UK), Prodromos Zanis (Greece)

Contributing Authors:
Wenche Aas (Norway), Dimitris Akritidis (Greece), Robert Allen (USA), Nicolas Bellouin (UK/France), Sara Marie Blichner (Norway), Josep G. Canadell (Australia), William Collins (UK), Owen Cooper (USA), Frank J. Dentener (EU/The Netherlands), Sarah Doherty (USA), Jean-Louis Dufresne (France), Sergio Henrique Faria (Spain/Brazil), Piers Forster (UK), Tzung-May Fu (China), Jan Sigurd Fuglestvedt (Norway), John C. Fyfe (Canada), Aristeidis K. Georgoulias (Greece), Matthew Gidden (Austria/USA), Nathan P. Gillett (Canada), Paul Ginoux (USA), Paul Griffiths (UK), Jian He (USA/China), Christopher Jones (UK), Svitlana Krakovska (Ukraine), Chaincy Kuo (USA), David S. Lee (UK), Maurice Levasseur (Canada), Martine Lizotte (Canada), Marianne Tronstad Lund (Norway), Jean-François Müller (Belgium), Helène Muri (Norway), Zebedee Nicholls (Australia), Jurgita Ovadnevaite (Ireland/Lithuania), Prabir Patra (Japan/India), Fabien Paulot (USA/France), Pallav Purohit (Austria/India), Johannes Quaas (Germany), Joeri Rogelj (Austria/Belgium), Bjørn Samset (Norway), Chris Smith (UK), Izuru Takayabu (Japan), Alexandra Tsimpidi (Germany/Greece), Steven Turnock (UK), Rita Van Dingenen (Belgium), Hua Zhang (China), Alcide Zhao (UK/China)

Review Editors:
Yugo Kanaya (Japan), Michael Prather (USA), Nourredine Yassaa (Algeria)

Chapter Scientist:
Chaincy Kuo (USA)

Date of Draft: 3 May 2021

Notes: TSU compiled version

Table of Contents

6.SM.1 Methodology for Emission based ERF 3
6.SM.2 ERF and GSAT timeseries from emulators for individual compounds over the historical period 3
6.SM.3 Regression coefficient of annual mean surface ozone and $PM_{2.5}$ against annual surface temperature change. 5
6.SM.4 Effect on GSAT of a one year pulse of present-day emissions after 20 and 100 years. 7
6.SM.5 Methodology to compute source sector apportionment for surface air pollutants using TM5-FASST 8
6.SM.6 Data Table 11
References 26

6.SM.1 Methodology for Emission based ERF

Emission-based ERFs are assessed (Figure 6.12) based on multi-model attribution experiments performed under AerChemMIP (Collins et al., 2017) and analyzed by (Thornhill et al., 2021). The attribution experiments are done with the precursors emissions individually perturbed (except CO and NMVOCs that were done together). Due to the non-linear chemistry and microphysics of the atmosphere, the sum of the emission-based contributions to ERF will not be equal to the concentration-based estimates (Figure 7.6)

The simulations in (Thornhill et al., 2021) are for the 1850-2014, and estimates for the emission-based ERFs have been extrapolated to the full 1750-2019 period based on the updated emission estimates from the 11 September 2020 version of the Community Emissions Data System (CEDS) is used (Hoesly et al., 2018), obtained from https://doi.org/10.5281/zenodo.4025316 (cf 7.SM.1.4)

For the ozone ERF, in the AerChemMIP experiments the methane concentrations have been kept fixed when the individual precursors are perturbed (e.g. NO_x). This means that methane is not governed by its emissions and the atmospheric chemistry. Thus, adjustments have been done to consider the differences between CH_4 concentrations that would have been reached in a free to adjust simulation and a CH_4-fixed simulation. As a consequence of this CH_4 adjustment, a correction has to be applied to all the chemical species which are affected by CH_4 modification, either through chemistry itself (e.g. lifetime) or through stratospheric H_2O changes and cloud changes. Despite these corrections, some non-linear effects in the chemistry can not be fully captured and result in differences between the emission-based radiative forcing and the concentration-based radiative forcing (Figure 7.6 and 7.SM.1.4). So finally, only the proportion of the individual effect is kept from this methodology and applied to the concentration-based ERF which has been determined in a way that allow to consider all the non-linearities.

The emission based ERF estimates for aerosols and aerosol precursors are based on the AerChemMIP simulations (Thornhill et al., 2021). The contribution from aerosol radiation interaction (ari) is calculated as the difference between the total ERF and ERFaci. Thus, the non-cloud adjustments are included as aerosol radiation interaction. For NH_3 emissions ERFaci was not available, the ERF is contributed only to aerosol radiation interaction. As for the ozone precursors, only the proportion of the individual effect is kept from this methodology and applied to the concentration-based ERF .

For CO_2 the fraction of CO_2 in the atmosphere originating from anthropogenic emissions of non-CO_2 emissions must be subtracted from the concentration based estimate. The sum of Carbon emissions over the historical period of CH_4, halocarbons, NMVOC + CO is estimated to be 6.6, 0.02, 26 Gt(C) respectively. This includes a rough assumption that 25%, 0%, 50%, 0% (CH_4, halocarbons, NMVOC, CO) of reactive intermediates such as formaldehyde are lost to deposition. Also assumes that 12% of methane C is still in the atmosphere as methane (Stevenson et al., 2013). Using the (Joos et al., 2013) CO_2 response function to convolve the time profile of emissions gives a rise in CO_2 of 110 ppb that is proportionally subtracted from the CO_2 total.
For the halogenated species, the ERFs for CFCs and HCFCs are taken from Thornhill et al. (2021), and adjusted to include emissions up to 2019. The ERF from HFCs, taken from the concentration-based estimates (7.SM.1.4) are added, neglecting small effects through changes in OH concentrations affecting HFC lifetime.

6.SM.2 ERF and GSAT timeseries from emulators for individual compounds over the historical period

GSAT change in response to ERF from SLCFs has been estimated using an emulator (see cross chapter box 7.1 and 7.SM.2) and presented in Figures 6.12, 6.15, 6.22 and 6.24. The emulator used is an impulse response function (IRF) based on the two-layer energy balance model.
When the ERF time series is known, the response in GSAT at time *t* is given by:

$$GSAT(t) = \int_{t'=0}^{t} ERF(t') \cdot IRF(t-t')dt'$$

Where t'=0 denotes the time when the emission perturbation started, e.g. anthropogenic emissions since 1750.

The IRF used here has been calibrated according to the procedure given in 7.SM.2, and is given by:

$$IRF(t) = \sum_{j=1}^{J} \frac{c_j}{d_j} \exp\left(-\frac{t}{d_j}\right)$$

where the parameters c_j determine the equilibrium climate response and d_j are timescales of the fast and slow modes of the climate system response, and J=2 here. The parameter values are: d_1 = 3.4 years and d_2 = 285 years, c_1 = 0.44 K/(W m^{-2}) and c_2 = 0.32 K/(W m^{-2}), corresponding to an ECS of 3.0K.

Figure 6.12 shows the historical emission based contributions to GSAT (1750-2019). For this analysis the emission based ERF time series are based on the AerChemMIP simulations (Thornhill et al., 2021), and described in 6.SM.1 and 7.SM.1.4. The emission-based assessment of ERF (6.SM.1) provides ERFs for 2019 relative to 1750, and to establish the ERF time series over the whole historical period, these were scaled back according the historic emissions, i.e. assuming a liner relation between emissions and ERF historically.

Figure 6.15 shows the GSAT response to step emission reductions of idealized climate forcers with different lifetimes. All forcers are assumed to give an ERF of -1.0 Wm^{-2} when a new equilibrium concentration is reached. With this assumption the ERF(t) is given by:

$$ERF(t) = -1.0\, Wm^{-2} \cdot (1 - e^{-\frac{t}{\tau}})$$

Where τ is the atmospheric lifetime of the climate forcer.

Figure 6.22 and 6.24 show the contributions to GSAT from individual SLCFs, or groups of SLCFs, with an abundance-based perspective. The ERF time series are from the assessment of chapter 7 of this report and details are given in 7.SM.1.4.

6.SM.3 Regression coefficient of annual mean surface ozone and $PM_{2.5}$ against annual surface temperature change.

[START FIGURE 6.SM.1 HERE]

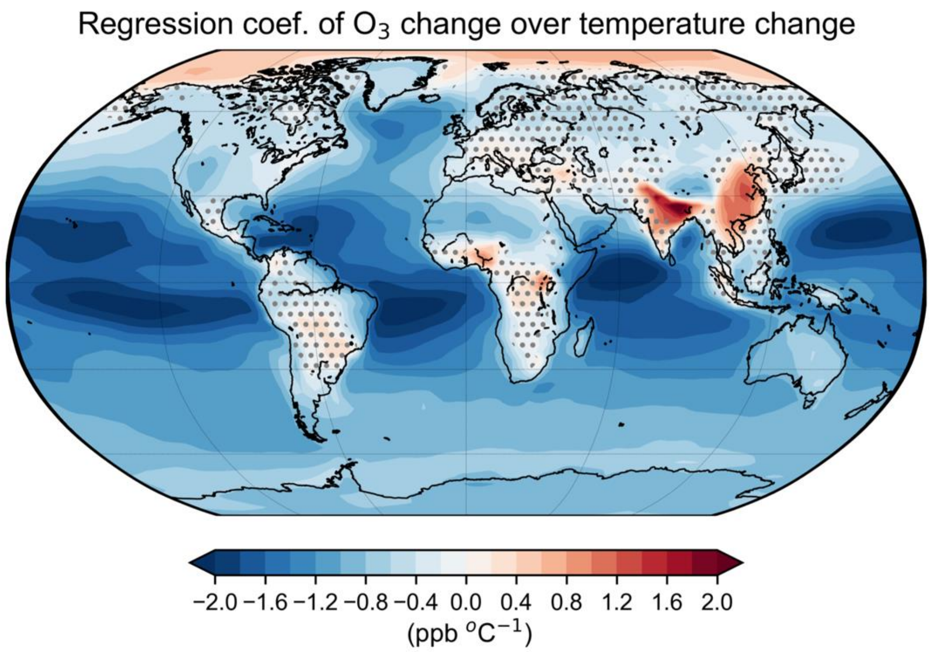

Figure 6.SM.1: Spatial pattern of the regression coefficient of annual surface ozone change (ssp370SST-ssp370pdSST) over annual surface temperature change (ssp370SST-ssp370pdSST) (ppb $^{o}C^{-1}$) during the time period from 2015 to 2100, for the CMIP6 ensemble average (GFDL-ESM4, GISS-E2-1-G, MRI-ESM2-0, UKESM1-0-LL). Regions without dots indicate that modelled regression coefficients are statistically significant (at the 95% significance level) and agree on the sign for at least three out of four models.

[END FIGURE 6.SM.1 HERE]

[START FIGURE 6.SM.2 HERE]

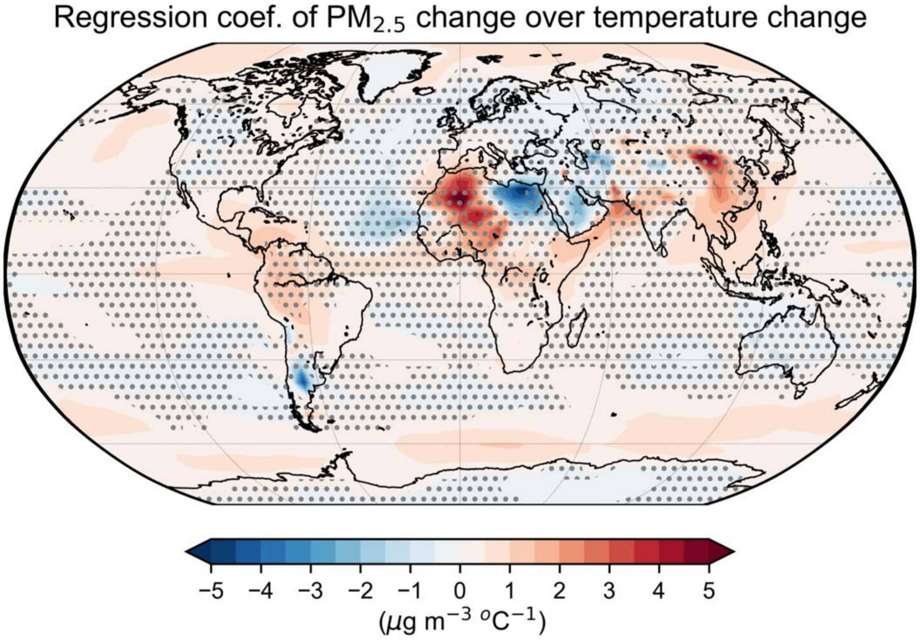

Figure 6.SM.2: Spatial pattern of the regression coefficient of annual surface $PM_{2.5}$ concentrations change (ssp370SST-ssp370pdSST) over annual surface temperature change (ssp370SST-ssp370pdSST) (µg m^{-3} $^{o}C^{-1}$) during the time period from 2015 to 2100, for the CMIP6 ensemble average (GFDL-ESM4, GISS-E2-1-G, MRI-ESM2-0). Regions without dots indicate that modelled regression coefficients are statistically significant (at the 95% significance level) and agree on the sign for at least two out of three models.

[END FIGURE 6.SM.2 HERE]

6.SM.4 Effect on GSAT of a one year pulse of present-day emissions after 20 and 100 years.

[START FIGURE 6.SM.3 HERE]

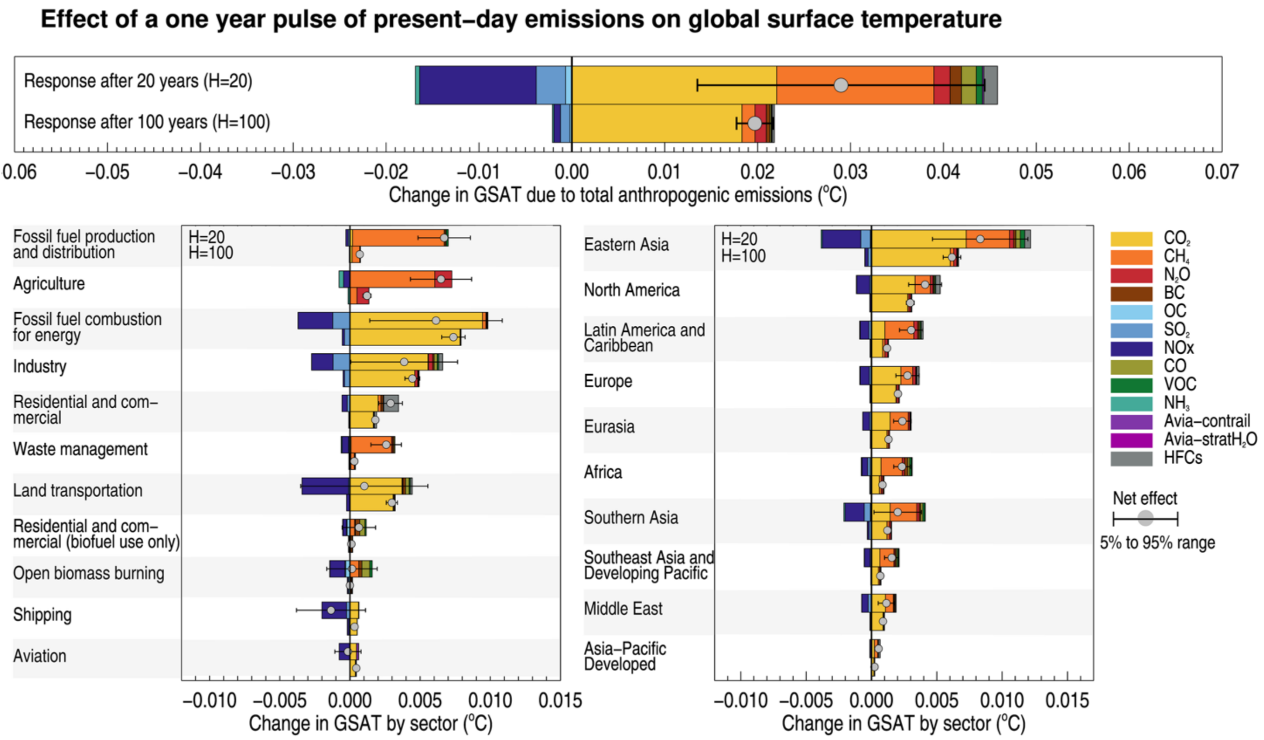

Figure 6.SM.3: Global-mean temperature response 20 and 100 years following one year of present-day (year 2014) emissions.

[END FIGURE 6.SM.3 HERE]

The temperature responses in Figure 6.16 and 6.SM.3 were calculated using the concept of absolute global temperature change potential (AGTP) (Shine et al., 2005), i.e., an emission-metric-based emulator of the climate response to individual emitted species. The approach and further details are documented in Lund et al. (2020). The emissions were taken from the Community Emissions Data System (CEDS) for year 2014 (Hoesly et al., 2018), with the exceptions of HFCs, which originate from Purohit et al. (2020) and consider HFCs with a lifetime shorter than 50 years, open biomass burning from van Marle et al. (2017), and aviation water vapour from Lee et al. (2020). The split between fossil fuel and biofuel emissions in the residential sector, and between the fossil fuel production and distribution and combustion in the energy sector, is based on the GAINS model (ECLIPSE version 6b dataset: https://iiasa.ac.at/web/home/research/researchPrograms/air/Global_emissions.html). CO_2 emissions are excluded from open biomass burning and residential biofuel use due to their unavailability in CEDS and uncertainties around non-sustainable emission fraction.

Aviation specific AGTPs have been calculated for Figure 6.SM.3 using the method described in Lund et al. (2020) and the best estimate radiative forcing values from Lee et al. (2020). For the HFCs , the AGTPs were derived from Hodnebrog et al. (2020). The AGTPs of BC, SO_2 and OC account for the direct aerosol effect due to aerosol-radiation interactions and are scaled to account for the semi-direct of BC due to rapid adjustments and indirect radiative forcing through aerosol-cloud interactions of sulfate aerosols, respectively. All AGTPs used in the temperature response calculations now include a carbon-climate feedback term based on the framework by Gasser et al. (2017), except those for HFCs. Avia-contrail refers to the impact from linear contrail formation and subsequent spreading to cirrus clouds and Avia-stratH_2O to the direct impact of aircraft water vapour emissions.

The error bars show the range (5-95% interval) in net temperature impact due to uncertainty in radiative forcing *only*. This uncertainty range is calculated using a Monte Carlo approach and estimates of uncertainties in global-mean RF of individual species from the literature - see Lund et al. (2020) for details. The uncertainty in the RF of individual halocarbons was not included due to lack of available data.

The AGTP applies an impulse response function (IRF) to calculate the temperature response as a function of time to a given forcing. The IRF is given by:

$$IRF(t) = \sum_{j=1}^{J} \frac{c_j}{d_j} \exp\left(-\frac{t}{d_j}\right)$$

where c_j and d_j are constants and timescales of the fast and slow model of the climate system response, respectively, and j=2 here. The IRF used in Lund et al. (2020) is based on Geoffroy et al. (2013), which yields d_1 = 4.1 years and d_2 = 249 years, c_1 = 0.519 K/(Wm^{-2}) and c_2 = 0.365 K/(Wm^{-2}), corresponding to an ECS of 3.5K. Note that the IRF used for calculations of GSAT for figures 6.12, 6.15, 6.22 and 6.24 use an IRF calibrated to the assessment of ECS and TCR as given in Chapter 7 of this report, and thus use slightly different values for the c_j and d_j constants (see 6.SM.2).

6.SM.5 Methodology to compute source sector apportionment for surface air pollutants using TM5-FASST

Here we provide description of the methodology used to calculate the source sector apportionment for $PM_{2.5}$ and ozone (Figure 6.17). Furthermore, Figures 6.SM4 and 6.SM.5 show a comparison of TM5-FASST and ESM models responses to changes in emissions of $PM_{2.5}$ precursors and ozone.

TM5-FASST is a reduced-form source-receptor model, describing the surface level spatial response of a pollutant metric (concentration, exposure, deposition) to changes in precursor emissions. The model is constructed from pre-computed emission-concentration transfer matrices between pollutant source regions and receptor regions. These matrices reflect underlying meteorological and chemical atmospheric processes for a predefined set of meteorological and emission data and have the advantage that concentration responses to emission changes are obtained by a simple matrix multiplication, avoiding expensive numerical computations.

TM5-FASST's source-receptor matrices have been derived with the chemistry-transport model TM5, by applying 20% emission perturbations on a reference emission set (RCP year 2000, year 2001 meteorology) for individual precursors and 56 source regions. The total concentration of component (or metric) *j* in receptor region *y*, resulting from given emissions *E* of *all* n_i precursors *i* at *all* n_x source regions *x*, is obtained as a perturbation on the base-simulation concentration, by summing up all the respective source-receptor coefficients A, scaled with the actual emission perturbation:

$$C_j(y) = C_{j,\mathrm{ref}}(y) + \sum_{k=1}^{n_x} \sum_{i=1}^{n_i} A_{ij}[x_k, y] \cdot \left[E_i(x_k) - E_{i,\mathrm{ref}}(x_k)\right] \quad (1)$$

where $A_{ij}[x_k, y] = \frac{\Delta C_{j,ref}(y)}{0.2 E_{i,\mathrm{ref}}(x_k)}$, the pre-computed source-receptor coefficient for source region x_k to receptor region y, for precursor i contributing to metric/pollutant j. The computational efficiency from the linearized emission-concentration sensitivities comes at some cost of accuracy, in particular because the model bypasses underlying mechanisms describing chemical and meteorological feedback processes that could lead to non-linear responses.

TM5-FASST computes $PM_{2.5}$ concentrations from precursor emissions of SO_2, NO_x, NH_3, elemental carbon and particulate organic matter. Secondary organic matter from anthropogenic emissions is not included. Ozone concentrations and long-term exposure metrics are computed from NO_x, non-methane volatile organic compounds (NMVOC) and methane precursor emissions. CO as ozone precursor is not included. The methane-ozone response is assumed to be instantaneous, neglecting the 11 year response time (Fiore et al., 2008)

The computational efficiency of TM5-FASST allows for multiple runs exploring source attribution by region or emission source. We estimate the relative contribution of individual emission sectors shown in Figure 6.17 by subtracting their emissions one by one from the total emissions in Eq. (1) and computing the resulting concentration. Subtracting this result from the total concentration (Eq. 1) yields each sector's contribution (Karagulian et al., 2016).

TM5-FASST has been extensively documented and evaluated by (Van Dingenen et al., 2018). The model has been applied in a variety of assessment studies (e.g., Aakre et al., 2018; Brauer et al., 2016; Crippa et al., 2019; Harmsen et al., 2020; Kühn et al., 2020; Markandya et al., 2018; Rao et al., 2017; Rauner et al., 2020; Vandyck et al., 2020). Validation studies in Van Dingenen et al. (2018) show that, despite inherent simplifications and caveats, large scale $PM_{2.5}$ and O_3 responses to emission changes in TM5-FASST compare well with the chemical transport model TM5. Figure 6.SM.4 and 6.SM.5 compare TM5-FASST regional $PM_{2.5}$ and O_3 responses to emission changes with the ensemble of ESM models for selected SSP scenarios. In nearly all cases TM5-FASST results fall within ±1 standard deviation of the CMIP6 ESM ensemble. Notable differences are observed for the SSP scenarios and regions representing more extreme emission changes (in particular for the low emission scenarios in Southern Asia). As documented by Van Dingenen et al. (2018), both for $PM_{2.5}$ and O_3 the differences with full process models can be attributed to non-linear responses to NO_x emission reductions that are not captured by the linearized source-receptor model.

[START FIGURE 6.SM.4 HERE]

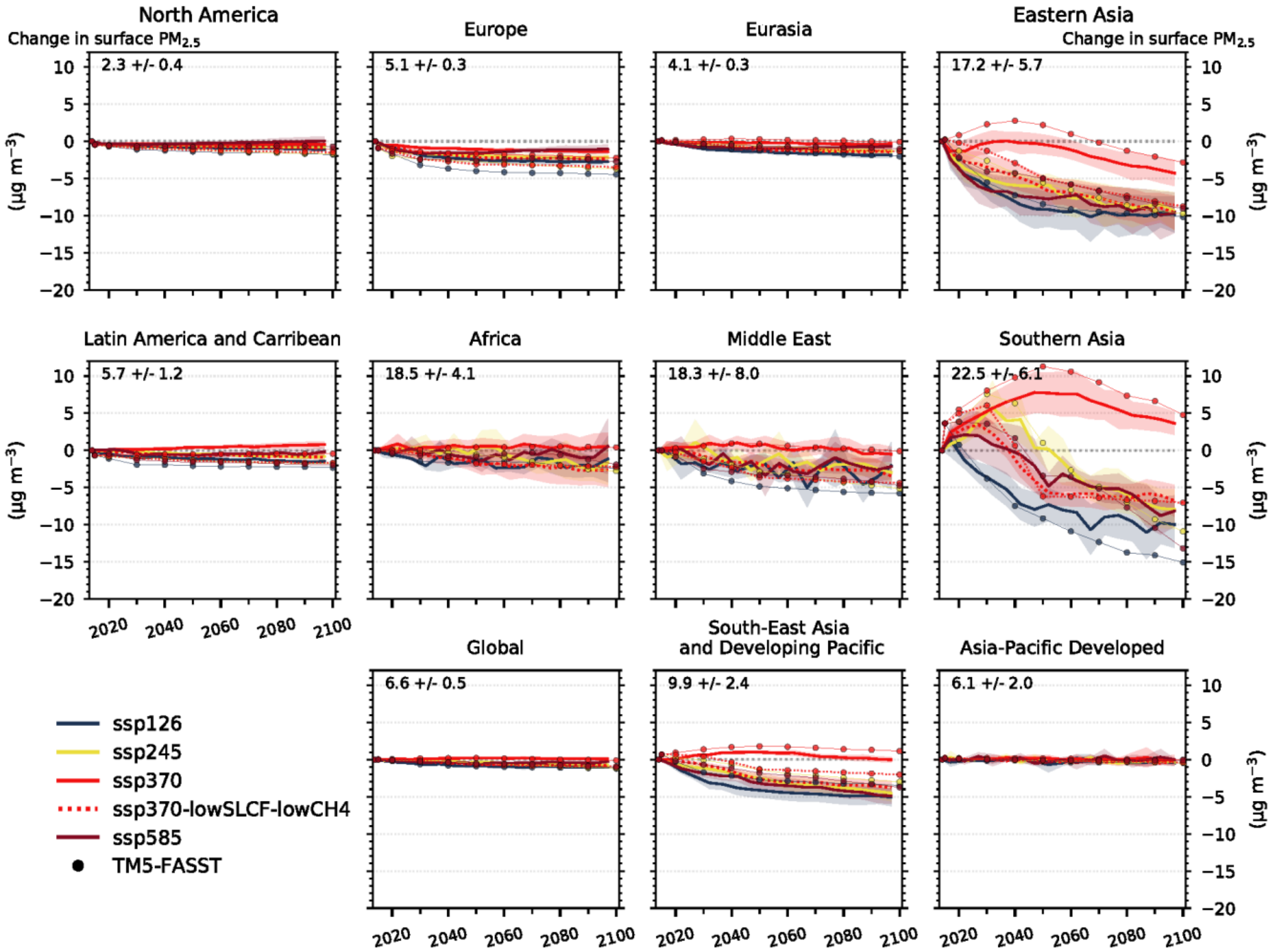

Figure 6.SM.4: Future global and regional changes in annual mean surface $PM_{2.5}$, relative to 2005-2014 mean, for the different SSPs used in CMIP6. Each line represents a multi-model mean across the region with shading representing the ± 1 standard deviation in the mean. Dots represent TM5-FASST results. The multi-model regional mean value (± 1 standard deviation) for the year 2005-2014 is shown in the top left corner of each panel.

[END FIGURE 6.SM.4 HERE]

[START FIGURE 6.SM.5 HERE]

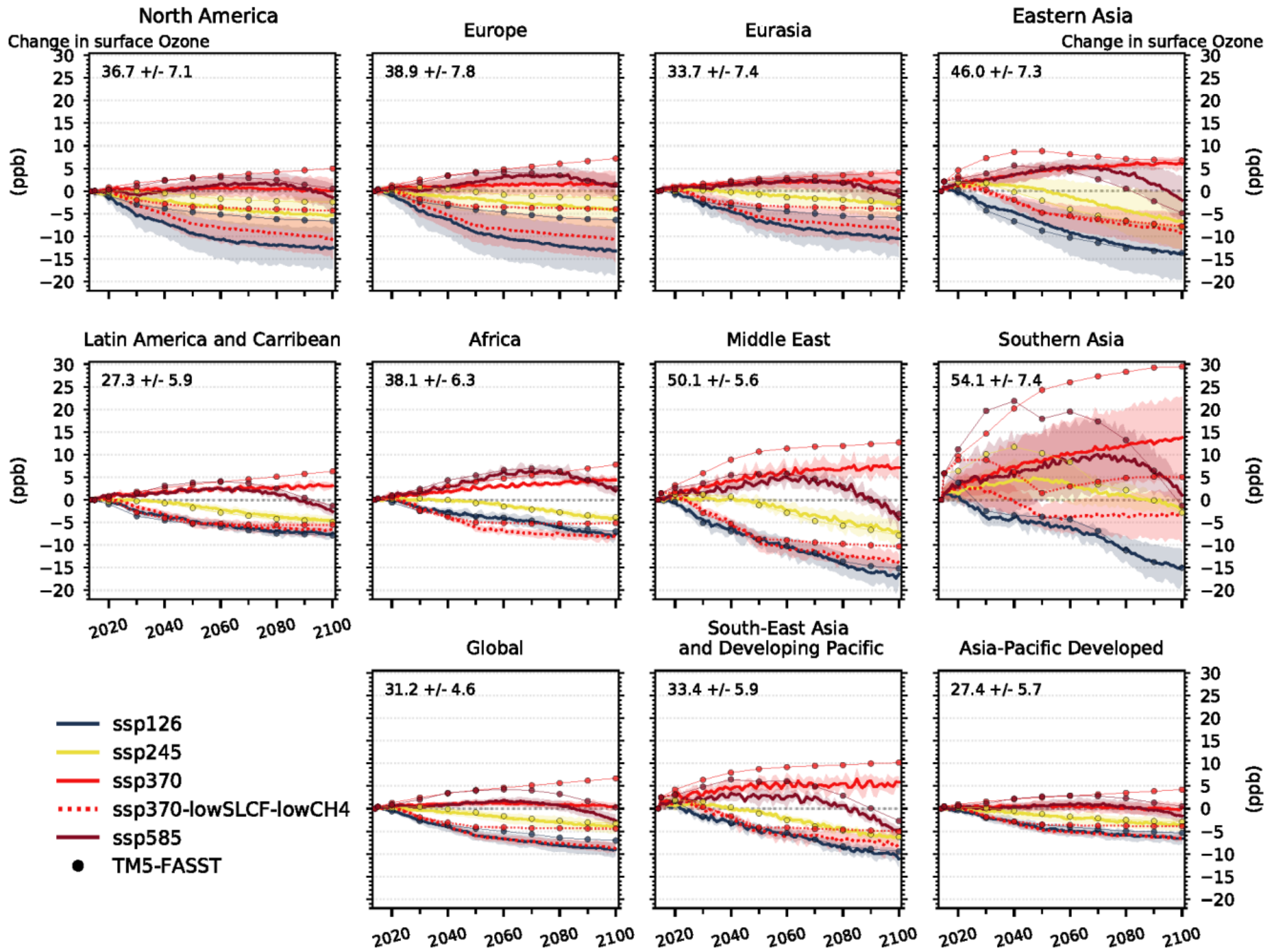

Figure 6.SM.5: Future global and regional changes in annual mean surface O3, relative to 2005-2014 mean, for the different SSPs used in CMIP6. Each line represents a multi-model mean across the region with shading representing the ± standard deviation in the mean. Dots represent TM5-FASST results. The multi-model regional mean value (± 1 standard deviation) for the year 2005-2014 is shown in the top left corner of each panel.

[END FIGURE 6.SM.5 HERE]

6.SM.6 Data Table

[START TABLE 6.SM.1 HERE]

Table 6.SM.1: Input Data Table. Input datasets and code used to create chapter figures.

Figure number/Table number/Chapter section (for calcuations)	Dataset name	Type of dataset	Filename	License type	Dataset citation	Dataset DOI/URL	Citation for relevant papers
Figure 6.3	Community Emissions Data System (CEDS)	Input dataset		Public	(Hoesly et al., 2018)	http://www.globalchange.umd.edu/ceds/	
Figure 6.4	CMIP6, ScenarioMIP, Tropospheric Ozone Assessment Report (TOAR), Atmospheric Chemistry and Climate Model Intercomparison Project (ACCMIP)	Input dataset	CMIP6 Models UKESM1-LL-0, CESM2-WACCM, GFDL-ESM4, MRI-ESM2-0,GISS-E2.1-G. Experiments : Historical experiment, ssp370	public	(Eyring et al., 2016; O'Neill et al., 2016)	https://esgf-node.llnl.gov/search/cmip6/	(Young et al., 2013, 2018; DuplicateGriffiths et al., 2020)
	Observational datasets TOST, IASI-FORLI, IASI-OFRID,OMI/MLS, OMI-SAI, OMI-RAL:	Input dataset		public		https://doi.org/10.1525/elementa.291.t1	(Gaudel et al., 2018)

	CMIP6 model data						
	CESM2-WACCM: historical, ssp370	Input dataset			(Danabasoglu, 2019b, 2019c)		
	GFDL-ESM4: esm-hist, historical, ssp370	Input dataset			(John et al., 2018c; Krasting et al., 2018b, 2018a)		
	GISS-E2-1-G: historical, ssp370	Input dataset			(NASA Goddard Institute for Space Studies (NASA/GISS), 2018, 2020h)		
	MRI-ESM2-0: historical, ssp370	Input dataset			(Yukimoto et al., 2019g, 2019c)		
	UKESM1-0-LL: historical, ssp370	Input dataset			(Good et al., 2019c; Tang et al., 2019)		
Figure 6.5	IAGOS-CORE	Input dataset	decadal	public	(Gaudel et al., 2020)	http://www.iagos-data.fr/portal.html#TimeseriesPlace:	(Cooper et al., 2020)
Figure 6.6	Merged GOME/SCIAMACHY/GOME-2 (TM4NO2A	Input dataset	GOME_SCIAMACHY_GOME2ab_TroposNO2_v2.3_041996-092017_temis.nc	public		http://www.temis.nl/airpollution/no2.html	(Georgoulias et al., 2019)

	version 2.3)						
Figure 6.7	EPA $PM_{2.5}$ aerosol component	Input dataset	Monthly-average 2000-2018	public		https://aqs.epa.gov/aqsweb/airdata/download_files.html.	(Solomon et al., 2014)
	IMPROVE aerosol	Input dataset	Monthly-average daily 2000-2018	public		http://views.cira.colostate.edu/fed/QueryWizard/Default.aspx	
	EMEP $PM_{2.5}$ aerosol component	Input dataset	Monthly-average 2000-2018	public		https://www.emep.int/	
	Network Center for EANET, EANET Data on the Acid Deposition in the East Asian Region, $PM_{2.5}$ aerosol component	Input dataset	Monthly-average 2001-2017	public		https://www.eanet.asia/document/public/index	
	SPARTAN $PM_{2.5}$ aerosol component	Input dataset	Monthly-average 2013-2019	public		https://www.spartan-network.org/	(Snider et al., 2015)
	observational field campaigns $PM_{2.5}$ aerosol component over Latin America and Caribbean, Africa, Europe, Eastern Asia, and Asia-Pacific Developed	Input dataset		public			(Celis et al., 2004; Feng et al., 2006; Mariani and de Mello, 2007; Molina et al., 2007, 2010; Bourotte et al., 2007; Fuzzi et al., 2007; Mkoma, 2008; Favez et al., 2008; Aggarwal and Kawamura, 2009; Mkoma et al., 2009; Li et al., 2010; Martin et al., 2010; Radhi et al., 2010; Weinstein et

							al., 2010; de Souza et al., 2010; Batmunkh et al., 2011; Pathak et al., 2011; Gioda et al., 2011; Zhang et al., 2012; Zhao et al., 2013; Cho and Park, 2013; Wang et al., 2019; Kuzu et al., 2020)
		Intermediate dataset				Code to be placed in https://github.com/IPCC-WG1	
Figure 6.8	CMIP6 Ambient Aerosol Optical Thickness at 550nm	Input dataset Annual average	historical experiment, Models ACCESS-CM2, BCC-ESM1, CESM2-FV2,CESM2-WACCM,CESM2,CNRM-CM6-1,CNRM-EMS2-1,CanESM5,E3SM-1-0,GFDL-CM4,GFDL-ESM4,GISS-E2-1-G,HadGEM3-GC31-LL,INM-CM4-8,IPSL-CM6A-LR,KACE-1-0-G,MIROC-ES2L,MPI-ESM-1-2,MPI-ESM1-2-HR,MPI-ESM1-2-LR,MRI-ESM2-0,NorESM2-LM,UKESM1-0-LL		(Eyring et al., 2016; O'Neill et al., 2016)		
Figure 6.9	CMIP6, mole fraction hydroxyl in air	Input dataset Decadal average	Models UKESM1-0LL, GFDL-ESM4, CESM2-WACCM	public	(Eyring et al., 2016)	https://esgf-node.llnl.gov/search/cmip6/	(Montzka et al., 2011; Rigby et al., 2017; Turner et al., 2017;

							Nicely et al., 2018; Naus et al., 2019; Patra et al., 2021)
	CMIP6 model data						
	CESM2-WACCM: historical	Input dataset			(Danabasoglu, 2019b)		
	GFDL-ESM4: historical	Input dataset			(Krasting et al., 2018b)		
	UKESM1-0-LL: historical	Input dataset			(Tang et al., 2019)		
Figure 6.10	CMIP6: AerChemMIP experiments histSST and histSST-piAer. Output variable rsut and rlut	Input dataset Averaged from monthly output	Models, MIROC6, MPI-I-ESM-1-2-HAM,GISS-E2-1-G, NorESM2-LM, MRI-ESM2-0, GFDL-ESM4, UKESM-0-LL	public	(Eyring et al., 2016; Collins et al., 2017)	https://esgf-node.llnl.gov/search/cmip6/	(Myhre et al., 2013)
		Intermediate dataset				Code to be placed in https://github.com/IPCC-WG1 TBD	
	CMIP6 model data						
	GFDL-ESM4: histSST, histSST-piAer	Input dataset			(Horowitz et al., 2018b, 2018a)		
	GISS-E2-1-G: histSST, histSST-piAer	Input dataset			(NASA Goddard Institute for Space Studies (NASA/GISS), 2019a, 2019b)		

	MIROC6: histSST, histSST-piAer	Input dataset			(Takemura, 2019a, 2019b)		
	MPI-ESM-1-2-HAM: histSST, histSST-piAer	Input dataset			(Neubauer et al., 2019b, 2019a)		
	MRI-ESM2-0: histSST, histSST-piAer	Input dataset			(Yukimoto et al., 2019a, 2020a)		
	NorESM2-LM: histSST, histSST-piAer	Input dataset			(Oliviè et al., 2019b, 2019a)		
	UKESM1-0-LL: histSST, histSST-piAer	Input dataset			(O'Connor, 2019b, 2019a)		
Figure 6.11	CMIP6: AerChemMIP experiments histSST and histSST-piAer. Output variable rsut and rlut	Input dataset Averaged from monthly output	Models, MIROC6, MPI-I-ESM-1-2-HAM,GISS-E2-1-G, NorESM2-LM, MRI-ESM2-0, GFDL-ESM4, UKESM-0-LL	public	(Eyring et al., 2016; Collins et al., 2017)	https://esgf-node.llnl.gov/search/cmip6/ Code to be placed in https://github.com/IPCC-WG1 TBD	(Myhre et al., 2013)
	Data citations						
	GFDL-ESM4: histSST, histSST-piAer	Input dataset			(Horowitz et al., 2018b, 2018a)		
	GISS-E2-1-G: histSST, histSST-piAer	Input dataset			(NASA Goddard Institute for Space Studies (NASA/GISS), 2019a,		

					2019b)		
	MIROC6: histSST, histSST-piAer	Input dataset			(Takemura, 2019a, 2019b)		
	MPI-ESM-1-2-HAM: histSST, histSST-piAer	Input dataset			(Neubauer et al., 2019b, 2019a)		
	MRI-ESM2-0: histSST, histSST-piAer	Input dataset			(Yukimoto et al., 2019a, 2020a)		
	NorESM2-LM: histSST, histSST-piAer	Input dataset			(Oliviè et al., 2019b, 2019a)		
	UKESM1-0-LL: histSST, histSST-piAer	Input dataset			(O'Connor, 2019b, 2019a)		
Figure 6.12	CMIP6,	Input dataset			(Eyring et al., 2016)	https://esgf-node.llnl.gov/search/cmip6/ Code to be placed in https://github.com/IPCC-WG1 TBD	(Ghan, 2013; DuplicateThornhill et al., 2021)
Figure 6.13	CMIP6: AerChemMIP experiments historical and hist-piAer. Output variable tas	Intermediate dataset	Models MIROC6, MRI-ESM2-0, NorESM2-LM, GFDL-ESM4, GISS-E2-1-G, UKESM1-0-LL.		(Eyring et al., 2016; Collins et al., 2017)	Code to be placed in https://github.com/IPCC-WG1 TBD	
Figure 6.14	CMIP6 historical experiment, AerChemMIP experiments ssp370 ssp370SST, ssp370pdSST experiments.	Input dataset Monthly mean	Models GFDL-ESM4, GISS-E2-1-G,MRI-ESM2-0,UKESM1-0-LL	public	(Eyring et al., 2016; Collins et al., 2017)	https://esgf-node.llnl.gov/search/cmip6/ Code to be placed in https://github.com/IPCC-WG1 TBD	

	Output variables o3, tas						
	Data citations						
	GFDL-ESM4: ssp370SST, ssp370pdSST	Input dataset			(Horowitz et al., 2018c, 2018d)		
	GISS-E2-1-G: ssp370SST, ssp370pdSST	Input dataset			(NASA Goddard Institute for Space Studies (NASA/GISS), 2020b, 2020a)		
	MRI-ESM2-0: ssp370SST, ssp370pdSST	Input dataset			(Yukimoto et al., 2019b, 2020b)		
	UKESM1-0-LL: ssp370pdSST, ssp370SST	Input dataset			(O'Connor, 2020b, 2020a)		
Figure 6.15	CMIP6, ScenarioMIP experiments ssp370SST, ssp370pdSST Mole fraction of ozone	Input dataset OUTPUT DATA FREQUENCY	Models GFDL-ESM4, GISS-E2-1-G, MRI-ESM2-0, UKESM1-0-LL	public	(Eyring et al., 2016; O'Neill et al., 2016)	https://esgf-node.llnl.gov/search/cmip6/	
Figure 6.16	CMIP6, ScenarioMIP experiments ssp370SST, ssp370pdSST	Input dataset OUTPUT DATA FREQUENCY	CMIP6 models GFDL-ESM4, GISS-E2-1-G, MRI-ESM2-0 and UKESM1-0-LL	public	(Eyring et al., 2016; O'Neill et al., 2016)	https://esgf-node.llnl.gov/search/cmip6/	

Figure 6.17	CMIP6, ScenarioMIP Mole fraction of ozone	Input dataset Intermediate data	GFDL-ESM4, BCC-ESM1, CESM2-WACCM and UKESM1-0-LL for ssp370, GFDL-ESM4, BCC-ESM1, and CESM2-WACCM for ssp370-lowNTCF, GFDL-ESM4 and UKESM1-0-LL for SSP1-2.6, SSP2-4.5 and SSP5-8.5	public	(Eyring et al., 2016; O'Neill et al., 2016)	https://esgf-node.llnl.gov/search/cmip6/	
Figure 6.20 **Figure 6.21**	GEIA/ACCENT gridded emissions	Input dataset		public		http:// geiacenter.org	(Lamarque et al., 2010)
	Community Emissions Data System (CEDS) for Historical Emissions	Input dataset		public	(van Marle et al., 2017; Hoesly et al., 2018)	http://www.globalchange.umd.edu/ceds/ http://esgf-node.llnl.gov/search/input4mips/	
	SSP Database (Shared Socioeconomic Pathways) - Version 2.0,	Input dataset		public	(Riahi et al., 2017; Rogelj et al., 2018; Gidden et al., 2019)	https://tntcat.iiasa.ac.at/SspDb/dsd	
	Representative Concentration Pathway (RCP) database	Input dataset		public	(van Vuuren et al., 2011)	ttps://tntcat.iiasa.ac.at/RcpDb/dsd	
		Intermediate dataset				https://github.com/gidden/ar6-wg1-ch6-emissions Code to be placed in https://github.com/IPCC-WG1	
	CMIP6 model data in Figure 6.20						
	BCC-ESM1: ssp370, ssp370-lowNTCF, historical	Input dataset			(Zhang et al., 2018, 2019b, 2019a)		
	CESM2-WACCM: ssp370-lowNTCF, historical, ssp370	Input dataset			(Danabasoglu, 2019a, 2019b,		

					2019c)		
	GFDL-ESM4: ssp370-lowNTCF, historical, ssp126, ssp245, ssp370, ssp585	Input dataset			(Horowitz et al., 2018a; John et al., 2018c, 2018d, 2018a, 2018b; Krasting et al., 2018b)		
	GISS-E2-1-G: historical, ssp126, ssp245, ssp370, ssp370-lowNTCF, ssp585	Input dataset			(NASA Goddard Institute for Space Studies (NASA/GISS), 2018, 2020i, 2020g, 2020e, 2020f, 2020h)		
	MRI-ESM2-0: historical, ssp126, ssp245, ssp370, ssp370-lowNTCF, ssp585	Input dataset			(Yukimoto et al., 2019d, 2019h, 2019f, 2019e, 2019g, 2019c)		
	UKESM1-0-LL: ssp370-lowNTCF, historical, ssp126, ssp245, ssp370, ssp585	Input dataset			(Good et al., 2019a, 2019d, 2019c, 2019b; Tang et al., 2019; Byun,		

					2020)		
	CMIP6 model data in Figure 6.21						
	BCC-ESM1: ssp370, ssp370-lowNTCF, historical	Input dataset			(Zhang et al., 2018, 2019b, 2019a)		
	CESM2-WACCM: ssp370-lowNTCF, historical, ssp370	Input dataset			(Danabasoglu, 2019a, 2019b, 2019c)		
	CNRM-ESM2-1: ssp370-lowNTCF, historical, ssp370	Input dataset			(Seferian, 2018, 2019; Voldoire, 2019)		
	GFDL-ESM4: ssp370-lowNTCF, historical, ssp126, ssp245, ssp370, ssp585	Input dataset			(Horowitz et al., 2018a; John et al., 2018c, 2018d, 2018a, 2018b; Krasting et al., 2018b)		
	GISS-E2-1-G: ssp370-lowNTCF, historical, ssp126, ssp245, ssp370, ssp585	Input dataset			(NASA Goddard Institute for Space Studies (NASA/GISS), 2018, 2020i, 2020g, 2020f, 2020a, 2020h)		
	HadGEM3-GC31-	Input			(Good,		

	LL: historical, ssp126, ssp245, ssp585	dataset			2019, 2020b, 2020a; Ridley et al., 2019)		
	MIROC-ES2L: historical, ssp126, ssp245, ssp370, ssp585	Input dataset			(Hajima et al., 2019; Tachiiri et al., 2019a, 2019b, 2019d, 2019c)		
	MPI-ESM-1-2-HAM: ssp370-lowNTCF, historical, ssp370	Input dataset			(Neubauer et al., 2019b, 2019a)		
	MRI-ESM2-0: ssp370-lowNTCF, historical, ssp126, ssp245, ssp370, ssp585	Input dataset			(Yukimoto et al., 2019h, 2019f, 2019e, 2019g, 2019c, 2019a)		
Figure 6.22	NorESM2-LM: ssp370-lowNTCF, historical, ssp126, ssp245, ssp370, ssp585	Input dataset			(Olivié et al., 2019; Seland et al., 2019e, 2019d, 2019c, 2019b, 2019a)	https://esgf-node.llnl.gov/search/cmip6/	
Figure 6.23	UKESM1-0-LL: ssp370-lowNTCF, historical, ssp126, ssp245, ssp370, ssp585	Input dataset			(Good et al., 2019a, 2019d, 2019c, 2019b; Tang et al., 2019;	https://esgf-node.llnl.gov/search/cmip6/	

					Byun, 2020)		
Figure 6.24	CMIP6, AerChemMIP Output variable rsut and rlut, monthly output ssp370SST and ssp370SST-lowNTCF	Input dataset	BCC-ESM1, CNRM-ESM2-1, CESM2-WACCM, and GFDL-ESM4.	public	(Eyring et al., 2016; Collins et al., 2017)	https://esgf-node.llnl.gov/search/cmip6/	
Figure 6.25	ScenarioMIP, RCMIP Emulator output	Input dataset		public	(Eyring et al., 2016; O'Neill et al., 2016; Nicholls et al., 2020)	https://esgf-node.llnl.gov/search/cmip6/	(Geoffroy et al., 2013)
Figure 6.26	ScenarioMIP Emulator output	Input dataset		public	(O'Neill et al., 2016)	https://esgf-node.llnl.gov/search/cmip6/	(DuplicateLund et al., 2020)
Figure 6.27	ScenarioMIP Emulator output	Input dataset		public	(O'Neill et al., 2016)	https://esgf-node.llnl.gov/search/cmip6/	
Figure 6.25 FGD						https://tntcat.iiasa.ac.at/SspDb/dsd	
Figure	**CMIP6 model data**						

6.SM.1	GFDL-ESM4: ssp370SST, ssp370pdSST	Input dataset			(Horowitz et al., 2018c, 2018d)		
	GISS-E2-1-G: ssp370SST, ssp370pdSST	Input dataset			(NASA Goddard Institute for Space Studies (NASA/GISS), 2020d, 2020c)		
	MRI-ESM2-0: ssp370SST, ssp370pdSST	Input dataset			(Yukimoto et al., 2019b, 2020b)		
	UKESM1-0-LL: ssp370pdSST, ssp370SST	Input dataset			(O'Connor, 2020c, 2020b)		
Figure 6.SM.2	CMIP6 model data						
	GFDL-ESM4: ssp370SST, ssp370pdSST	Input dataset			(Horowitz et al., 2018c, 2018d)		
	GISS-E2-1-G: ssp370SST, ssp370pdSST	Input dataset			(NASA Goddard Institute for Space Studies (NASA/GISS), 2020d, 2020c)		
	MRI-ESM2-0: ssp370SST, ssp370pdSST	Input dataset			(Yukimoto et al., 2019b, 2020b)		

	UKESM1-0-LL: ssp370pdSST, ssp370SST	Input dataset			(O'Connor, 2020c, 2020b)		
Figure 6.SM.4	CMIP6 model data						
	GFDL-ESM4: ssp370-lowNTCFCH4	Input dataset			(Horowitz et al., 2018b)		
	GISS-E2-1-G: ssp370-lowNTCFCH4	Input dataset			(NASA Goddard Institute for Space Studies (NASA/GISS), 2020b)		
	MRI-ESM2-0: ssp370-lowNTCFCH4	Input dataset			(Yukimoto et al., 2020a)		
	UKESM1-0-LL: ssp370-lowNTCFCH4	Input dataset			(O'Connor, 2020a)		

[END TABLE 6.SM.6 HERE]

References

Aakre, S., Kallbekken, S., Van Dingenen, R., and Victor, D. G. (2018). Incentives for small clubs of Arctic countries to limit black carbon and methane emissions. *Nat. Clim. Chang.* doi:10.1038/s41558-017-0030-8.

Brauer, M., Freedman, G., Frostad, J., van Donkelaar, A., Martin, R. V, Dentener, F., et al. (2016). Ambient Air Pollution Exposure Estimation for the Global Burden of Disease 2013. *Environ. Sci. Technol.* 50, 79–88. doi:10.1021/acs.est.5b03709.

Collins, W. J., Lamarque, J. F., Schulz, M., Boucher, O., Eyring, V., Hegglin, I. M., et al. (2017). AerChemMIP: Quantifying the effects of chemistry and aerosols in CMIP6. *Geosci. Model Dev.* 10, 585–607. doi:10.5194/gmd-10-585-2017.

Crippa, M., Janssens-Maenhout, G., Guizzardi, D., Van Dingenen, R., and Dentener, F. (2019). Contribution and uncertainty of sectorial and regional emissions to regional and global PM$_{2.5}$ health impacts. *Atmos. Chem. Phys.* 19, 5165–5186. doi:10.5194/acp-19-5165-2019.

Fiore, A. M., West, J. J., Horowitz, L. W., Naik, V., and Schwarzkopf, M. D. (2008). Characterizing the tropospheric ozone response to methane emission controls and the benefits to climate and air quality. *J. Geophys. Res. Atmos.* doi:10.1029/2007JD009162.

Fuglestvedt, J. S., Shine, K. P., Berntsen, T., Cook, J., Lee, D. S., Stenke, A., et al. (2010). Transport impacts on atmosphere and climate: Metrics. *Atmos. Environ.* 44, 4648–4677. doi:10.1016/j.atmosenv.2009.04.044.

Gasser, T., Peters, G. P., Fuglestvedt, J. S., Collins, W. J., Shindell, D. T., and Ciais, P. (2017). Accounting for the climate–carbon feedback in emission metrics. *Earth Syst. Dyn.* 8, 235–253. doi:10.5194/esd-8-235-2017.

Geoffroy, O., Saint-Martin, D., Olivié, D. J. L., Voldoire, A., Bellon, G., and Tytéca, S. (2013). Transient Climate Response in a Two-Layer Energy-Balance Model. Part I: Analytical Solution and Parameter Calibration Using CMIP5 AOGCM Experiments. *J. Clim.* 26, 1841–1857. doi:10.1175/JCLI-D-12-00195.1.

Harmsen, M. J. H. M., van Dorst, P., van Vuuren, D. P., van den Berg, M., Van Dingenen, R., and Klimont, Z. (2020). Co-benefits of black carbon mitigation for climate and air quality. *Clim. Change*. doi:10.1007/s10584-020-02800-8.

Hodnebrog, Ø., Aamaas, B., Fuglestvedt, J. S., Marston, G., Myhre, G., Nielsen, C. J., et al. (2020). Updated Global Warming Potentials and Radiative Efficiencies of Halocarbons and Other Weak Atmospheric Absorbers. *Rev. Geophys.* 58, e2019RG000691. doi:https://doi.org/10.1029/2019RG000691.

Hoesly, R. M., Smith, S. J., Feng, L., Klimont, Z., Janssens-Maenhout, G., Pitkanen, T., et al. (2018). Historical (1750-2014) anthropogenic emissions of reactive gases and aerosols from the Community Emissions Data System (CEDS). *Geosci. Model Dev.* 11, 369–408. doi:10.5194/gmd-11-369-2018.

Joos, F., Roth, R., Fuglestvedt, J. S., Peters, G. P., Enting, I. G., von Bloh, W., et al. (2013). Carbon dioxide and climate impulse response functions for the computation of greenhouse gas metrics: a multi-model analysis. *Atmos. Chem. Phys.* 13, 2793–2825. doi:10.5194/acp-13-2793-2013.

Karagulian, F., Van Dingenen, R., Belis, C. A., Janssens-Maenhout, G., Crippa, M., Guizzardi, D., et al. (2016). Attribution of anthropogenic PM2. 5 to emission sources: : A global analysis of source-receptor model results and measured source-apportionment data (No. EUR 28510 EN), JRC Technical Reports. Ispra.

Kühn, T., Kupiainen, K., Miinalainen, T., Kokkola, H., Paunu, V.-V., Laakso, A., et al. (2020). Effects of black carbon mitigation on Arctic climate. *Atmos. Chem. Phys.* 20, 5527–5546. doi:10.5194/acp-20-5527-2020.

Lee, D. S., Fahey, D. W., Skowron, A., Allen, M. R., Burkhardt, U., Chen, Q., et al. (2020). The contribution of global aviation to anthropogenic climate forcing for 2000 to 2018. *Atmos. Environ.*, 117834. doi:10.1016/j.atmosenv.2020.117834.

Lund, M. T., Aamaas, B., Stjern, C. W., Klimont, Z., Berntsen, T. K., and Samset, B. H. (2020). A continued role of Short-Lived Climate Forcers under the Shared Socioeconomic Pathways. *Earth Syst. Dyn.* 11, 977–993. doi:10.5194/esd-11-977-2020.

Markandya, A., Sampedro, J., Smith, S. J., Van Dingenen, R., Pizarro-Irizar, C., Arto, I., et al. (2018). Health co-benefits from air pollution and mitigation costs of the Paris Agreement: a modelling study. *Lancet Planet. Heal.* 2, e126–e133. doi:10.1016/S2542-5196(18)30029-9.

Purohit, P., Höglund-Isaksson, L., Dulac, J., Shah, N., Wei, M., Rafaj, P., et al. (2020). Electricity savings and greenhouse gas emission reductions from global phase-down of hydrofluorocarbons. *Atmos. Chem. Phys.* 20, 11305–11327. doi:10.5194/acp-20-11305-2020.

Rao, S., Klimont, Z., Smith, S. J., Van Dingenen, R., Dentener, F., Bouwman, L., et al. (2017). Future air pollution in the Shared Socio-economic Pathways. *Glob. Environ. Chang.* 42, 346–358. doi:10.1016/j.gloenvcha.2016.05.012.

Rauner, S., Bauer, N., Dirnaichner, A., Dingenen, R. Van, Mutel, C., and Luderer, G. (2020). Coal-exit health and environmental damage reductions outweigh economic impacts. *Nat. Clim. Chang.* 10, 308–312. doi:10.1038/s41558-020-0728-x.

Shine, K. P., Fuglestvedt, J. S., Hailemariam, K., and Stuber, N. (2005). Alternatives to the Global Warming Potential for Comparing Climate Impacts of Emissions of Greenhouse Gases. *Clim. Change* 68, 281–302. doi:10.1007/s10584-005-1146-9.

Stevenson, D. S., Young, P. J., Naik, V., Lamarque, J.-F., Shindell, D. T., Voulgarakis, A., et al. (2013). Tropospheric ozone changes, radiative forcing and attribution to emissions in the Atmospheric Chemistry and Climate Model Intercomparison Project (ACCMIP). *Atmos. Chem. Phys.* 13, 3063–3085. doi:10.5194/acp-13-3063-2013.

Thornhill, G. D., Collins, W. J., Kramer, R. J., Olivié, D., Skeie, R. B., O'Connor, F. M., et al. (2021). Effective radiative forcing from emissions of reactive gases and aerosols – a multi-model comparison. *Atmos. Chem. Phys.* 21, 853–874. doi:10.5194/acp-21-853-2021.

Van Dingenen, R., Dentener, F., Crippa, M., Leitao, J., Marmer, E., Rao, S., et al. (2018). TM5-FASST: a global atmospheric source--receptor model for rapid impact analysis of emission changes on air quality and short-lived climate pollutants. *Atmos. Chem. Phys.* 18, 16173–16211. doi:10.5194/acp-18-16173-2018.

van Marle, M. J. E., Kloster, S., Magi, B. I., Marlon, J. R., Daniau, A.-L., Field, R. D., et al. (2017). Historic global biomass burning emissions for CMIP6 (BB4CMIP) based on merging satellite observations with proxies and fire models (1750–2015). *Geosci. Model Dev.* 10, 3329–3357. doi:10.5194/gmd-10-3329-2017.

Vandyck, T., Keramidas, K., Tchung-Ming, S., Weitzel, M., and Van Dingenen, R. (2020). Quantifying air quality co-benefits of climate policy across sectors and regions. *Clim. Change* 163, 1501–1517. doi:10.1007/s10584-020-02685-7.